

# Phase formation, crystal chemistry, and properties in the system $\text{Bi}_2\text{O}_3\text{--Fe}_2\text{O}_3\text{--Nb}_2\text{O}_5$

Michael W. Lufaso<sup>a,1</sup>, Terrell A. Vanderah<sup>a,\*</sup>, Ileana M. Pazos<sup>a</sup>, Igor Levin<sup>a</sup>, Robert S. Roth<sup>a</sup>,  
Juan C. Nino<sup>b</sup>, Virgil Provenzano<sup>a</sup>, Peter K. Schenck<sup>a</sup>

<sup>a</sup>National Institute of Standards and Technology, Materials Science & Engineering Laboratory, Gaithersburg, MD 20899, USA

<sup>b</sup>Department of Materials Science & Engineering, University of Florida, Gainesville, FL 32611-6400, USA

Received 17 July 2006; accepted 22 August 2006

Available online 9 September 2006

## Abstract

Subsolidus phase relations have been determined for the  $\text{Bi}_2\text{O}_3\text{--Fe}_2\text{O}_3\text{--Nb}_2\text{O}_5$  system in air (900–1075 °C). Three new ternary phases were observed— $\text{Bi}_3\text{Fe}_{0.5}\text{Nb}_{1.5}\text{O}_9$  with an Aurivillius-type structure, and two phases with approximate stoichiometries  $\text{Bi}_{17}\text{Fe}_2\text{Nb}_{31}\text{O}_{106}$  and  $\text{Bi}_{17}\text{Fe}_3\text{Nb}_{30}\text{O}_{105}$  that appear to be structurally related to  $\text{Bi}_8\text{Nb}_{18}\text{O}_{57}$ . The fourth ternary phase found in this system is pyrochlore ( $A_2B_2O_6O'$ ), which forms an extensive solid solution region at Bi-deficient stoichiometries (relative to  $\text{Bi}_2\text{FeNbO}_7$ ) suggesting that  $\approx 4\text{--}15\%$  of the *A*-sites are occupied by  $\text{Fe}^{3+}$ . X-ray powder diffraction data confirmed that all Bi–Fe–Nb–O pyrochlores form with positional displacements, as found for analogous pyrochlores with Zn, Mn, or Co instead of Fe. A structural refinement of the pyrochlore 0.4400:0.2700:0.2900  $\text{Bi}_2\text{O}_3\text{:Fe}_2\text{O}_3\text{:Nb}_2\text{O}_5$  using neutron powder diffraction data is reported with the *A* cations displaced (0.43 Å) to 96*g* sites and *O'* displaced (0.29 Å) to 32*e* sites ( $\text{Bi}_{1.721}\text{Fe}_{0.190}(\text{Fe}_{0.866}\text{Nb}_{1.134})\text{O}_7$ , *Fd* $\bar{3}m$  (#227), *a* = 10.508(1) Å). This displacive model is somewhat different from that reported for  $\text{Bi}_{1.5}\text{Zn}_{0.92}\text{Nb}_{1.5}\text{O}_{6.92}$ , which exhibits twice the concentration of small *B*-type cations on the *A*-sites as the Fe system. Bi–Fe–Nb–O pyrochlores exhibited overall paramagnetic behavior with large negative Curie–Weiss temperature intercepts, slight superparamagnetic effects, and depressed observed moments compared to high-spin, spin-only values. The single-phase pyrochlore with composition  $\text{Bi}_{1.657}\text{Fe}_{1.092}\text{Nb}_{1.150}\text{O}_7$  exhibited low-temperature dielectric relaxation similar to that observed for  $\text{Bi}_{1.5}\text{Zn}_{0.92}\text{Nb}_{1.5}\text{O}_{6.92}$ ; at 1 MHz and 200 K the relative permittivity was 125, and above 350 K conductive effects were observed.

Published by Elsevier Inc.

**Keywords:**  $\text{Bi}_2\text{O}_3\text{--Fe}_2\text{O}_3\text{--Nb}_2\text{O}_5$ ; Phase equilibria; Phase diagram; Pyrochlore; Displacive disorder; Bismuth iron niobates; Bi–Fe–Nb–O; Dielectric properties; Magnetic properties

## 1. Introduction

Multiferroic materials which exhibit magnetoelectric effects have attracted considerable attention owing to their scientific interest as well as exciting possibilities for practical applications [1]. These multifunctional materials display ill-understood coupling between cooperative phenomena such as ferroelectricity and ferromagnetism. The possibility of manipulating the magnetic or dielectric properties of a single

material by an applied electric or magnetic field, respectively, opens up entirely new device applications in microelectronics and data storage [2–4]. Only a few compounds are known to exhibit the coexistence of ferromagnetism (or ferrimagnetism), ferroelectricity, and magnetoelectric coupling [3,5]. These include several perovskite-related compounds such as  $\text{BiFeO}_3$  [3,6],  $\text{BiMnO}_3$  [7],  $\text{YMnO}_3$  [8],  $\text{TbMnO}_3$  [9],  $\text{HoMnO}_3$  [10], and  $\text{Bi}_2\text{NiMnO}_6$  [11]. Currently, however, single-phase materials with magnetoelectric properties sufficiently robust for practical exploitation are not known. The present study of the  $\text{Bi}_2\text{O}_3\text{--Fe}_2\text{O}_3\text{--Nb}_2\text{O}_5$  system was undertaken to reveal compound formation among strongly polarizable and magnetic cations, and to elucidate the phase equilibria of  $\text{BiFeO}_3$  in the presence of  $\text{Nb}_2\text{O}_5$ .

\*Corresponding author. Fax: +1 301 975 5334.

E-mail address: [terrell.vanderah@nist.gov](mailto:terrell.vanderah@nist.gov) (T.A. Vanderah).

<sup>1</sup>Permanent address: Department of Chemistry & Physics, University of North Florida, Jacksonville, FL 32224.

## 2. Experimental methods

Sixty-eight polycrystalline specimens (3–4 g each) were prepared in air by solid-state reactions using  $\text{Bi}_2\text{O}_3$  (99.999%),  $\text{Fe}_2\text{O}_3$  (reagent grade), and  $\text{Nb}_2\text{O}_5$  (99.999%). Prior to each heating, each sample was mixed by grinding with an agate mortar and pestle for 15 min, pelletized, and placed on a bed of sacrificial powder of the same composition supported on alumina ceramic. After an initial overnight calcine at 800 °C (below the m.p. of  $\text{Bi}_2\text{O}_3$ , 825 °C) multiple 1–3 d heatings (with intermediate grinding and re-pelletizing) were carried out at 900–1075 °C.<sup>2</sup> Samples were furnace-cooled to ~700 °C and then air-quenched on the bench-top. Metastable melting in non-equilibrated ternary specimens (an initial problem owing to large differences in the melting points of  $\text{Bi}_2\text{O}_3$ ,  $\text{Fe}_2\text{O}_3$ , and  $\text{Nb}_2\text{O}_5$ ) was avoided by soaking samples at 900 °C for 1–3 d for the second heating, followed by a third heating at 970 °C for 1–3 d. Equilibrium was presumed when no further changes could be detected in the weakest peaks observed in the X-ray powder diffraction patterns.  $\text{Bi}_2\text{O}_3$  volatilization was observed above the solidus by thermogravimetric analysis, but was not detectable in the subsolidus study.

Pyrochlore-type crystals were readily grown by heating a single-phase polycrystalline specimen (composition 44:27:29  $\text{Bi}_2\text{O}_3$ : $\text{Fe}_2\text{O}_3$ : $\text{Nb}_2\text{O}_5$ ) in a Pt capsule (sealed by welding) to 1300 °C, followed by slow-cooling (5 °C/h) to below the freezing point (~1190 °C). The crystals were obtained as reddish orange shards and exhibited conchoidal fracture. The refined unit cell parameter obtained for a powdered sample of the crystals ( $a = 10.497(1)$  Å) was comparable to that of the starting material ( $a = 10.508(1)$  Å), suggesting similar Bi-contents. Pyrochlore films were readily deposited by pulsed laser deposition (248 nm KrF EXCIMER, 10 Hz, 10 J/cm<sup>2</sup>, background pressure 24 Pa O<sub>2</sub>) from a target disk prepared by sintering (1200 °C, 8 h) single-phase pyrochlore powder (composition 44:27:29  $\text{Bi}_2\text{O}_3$ : $\text{Fe}_2\text{O}_3$ : $\text{Nb}_2\text{O}_5$ ). Films grew at high deposition rates (~0.4 nm/s) on Si and Pt-coated Si substrates. Crystalline, highly <111> textured films were obtained by either cold deposition in vacuum, followed by annealing for 10 min at 700 °C, or by deposition at 600 °C in 17 Pa O<sub>2</sub>.

Phase assemblages were ascertained using the disappearing phase method [12,13] and X-ray powder diffraction data obtained with a Philips<sup>3</sup> diffractometer equipped with incident Soller slits, a theta-compensating slit and graphite

monochromator, and a scintillation detector. Samples were mounted in wetted glass slides. Patterns were collected at ambient temperatures using  $\text{CuK}\alpha$  radiation over the range 3–70°  $2\theta$  with a 0.02°  $2\theta$  step size and a 2 s count time. Intensity data measured as relative peak heights above background were obtained using the DATASCAN software package, and processed using JADE. For unit cell refinements, observed  $2\theta$  line positions were first corrected using SRM 660,  $\text{LaB}_6$  [14], as an external calibrant. Lattice parameters were refined using JADE ( $2\theta$  values,  $\text{CuK}\alpha_1 = 1.540593$  Å). Single pyrochlore-type crystals were characterized by the precession camera method (Zr-filtered  $\text{MoK}\alpha$  radiation) to assess quality, cell parameter, and space group.

Neutron powder diffraction data were collected using the BT-1 32-detector neutron powder diffractometer at the NIST Center for Neutron Research, NBSR. The specimen (~15 g) was loaded in a vanadium container of length 50 mm and diameter 12.4 mm. A  $\text{Cu}(311)$  monochromator with a 90° take-off angle,  $\lambda = 1.5402(2)$  Å, and in-pile collimation of 15 min of arc were used. Data were collected at 293 and at 10 K, over the range of 3–168°  $2\theta$  with a step size of 0.05°. The instrument is described at the website <http://www.ncnr.nist.gov/>.

The oxidation state of Fe in selected samples was evaluated by electron energy loss spectroscopy (EELS) using polycrystalline specimens that were crushed in acetone and dispersed on lacey carbon-coated grids. Measurements of the Fe- $L_{2,3}$  energy-loss near-edge structure (ELNES) were conducted in a JEOL-3010 UHR (300 kV) transmission electron microscope (TEM) equipped with a  $\text{LaB}_6$  electron source, Gatan Imaging Filter (GIF), and a slow-scan charge-coupled device (CCD) camera. The EELS spectra exhibiting the Fe- $L_{2,3}$  edge and the low-loss region were recorded with the TEM operated in the diffraction mode using a strongly under-saturated electron source, a 2 mm GIF entrance aperture, and an energy dispersion of 0.1 eV/channel (the full-width at half maximum of the zero-loss peak was 1.2 eV). Total integration times for the Fe- $L_{2,3}$  edge and the low-loss region were 50 and 1 s, respectively.  $\text{Fe}_2\text{O}_3$  (hematite) and  $\text{FeTiO}_3$  (ilmenite) were analyzed as references. For each sample, 10–15 spectra were collected from distinct particulates. The averaged background-subtracted spectra were processed to remove the effect of plural inelastic scattering using a Fourier-ratio deconvolution method [15]. The exposure of the sample to the electron beam was minimized to avoid radiation damage.

Magnetic properties were characterized using a Quantum Design SQUID magnetometer and single-phase polycrystalline samples. Magnetization was measured as a function of temperature between 2 and 300 K after cooling in the absence of an applied field (zero-field cooled, ZFC) and after cooling in a magnetic field (field-cooled, FC) of 50 kG. In addition, measurements at 4.2 and 300 K were carried out to determine the field dependence of the magnetization in applied fields between 0 and 50 kG.

<sup>2</sup>Exceptions: Specimens with Bi contents >60 mol% were not heated above 800 °C, to avoid decomposition of sillenite-type phases, and melting. A eutectic in the ternary system may occur near 50:25:25  $\text{Bi}_2\text{O}_3$ : $\text{Fe}_2\text{O}_3$ : $\text{Nb}_2\text{O}_5$ , which formed liquid at 950 °C; specimens near this composition were not heated above 925 °C.

<sup>3</sup>Certain commercial equipment and software are identified in order to adequately specify the experimental procedure; recommendation or endorsement by the National Institute of Standards and Technology is not therein implied.

Dielectric properties were measured using disks ( $\sim 13$  mm in diameter, 1 mm thick) pressed from single-phase powder and sintered at  $1025^\circ\text{C}$  for 4 h. Density was determined geometrically. Specimens were then polished to obtain planar surfaces and gold electrodes ( $\approx 75$  nm thick) were sputtered onto the pellet surfaces to form parallel plate capacitors. The capacitance and dielectric loss were measured using an Agilent 4284 LCR meter at frequencies varying from 1 kHz to 1 MHz. Reported permittivity data have been corrected to theoretical density. The sample temperature was varied between 110 and 475 K using a programmable 9023 Delta Design controller. Typical uncertainties in the permittivity data are on the order of 5% and are dominated by the geometric estimates of porosity.

### 3. Results and discussion

#### 3.1. Phase formation

The results of the phase equilibrium study are presented in Fig. 1. In the binary subsystem  $\text{Fe}_2\text{O}_3$ – $\text{Nb}_2\text{O}_5$ , the compounds  $\text{FeNbO}_4$  and  $\text{FeNb}_{11}\text{O}_{29}$  were observed [16,17]; solid solution around  $\text{FeNbO}_4$  was not detected. In the  $\text{Bi}_2\text{O}_3$ – $\text{Fe}_2\text{O}_3$  system [16] three compounds formed:

$\text{Bi}_2\text{Fe}_4\text{O}_9$  [18], which adopts a framework-type structure built from chains of edge-sharing  $[\text{FeO}_6]$  octahedra and pairs of vertex-sharing  $[\text{FeO}_4]$  tetrahedra;  $\text{BiFeO}_3$  [6,19–21], with a rhombohedrally distorted perovskite structure; and a sillenite-type phase  $\text{Bi}_{25}\text{FeO}_{40}$  [22]. Multi-ferroic  $\text{BiFeO}_3$  formed readily in phase assemblages in the ternary study, but could not be synthesized as a single phase; on-composition specimens always contained small amounts of  $\text{Bi}_2\text{Fe}_4\text{O}_9$  and  $\text{Bi}_{25}\text{FeO}_{40}$  whose phase fractions remained constant despite repeated grinding and hundreds of hours of heating at  $800^\circ\text{C}$ . Single-phase polycrystalline  $\text{BiFeO}_3$  has been reportedly obtained, however, by acid-leaching equilibrated two-phase samples of  $\text{BiFeO}_3$  and  $\text{Bi}_2\text{O}_3$  [23]. The binary Bi–Nb–O phases observed were in general agreement with the comprehensive study reported by Roth [24] except for the high- $\text{Bi}_2\text{O}_3$  ( $\geq 0.75$  mole fraction) region, represented in Fig. 1 as a “fluorite” solid solution extending from 75:25  $\text{Bi}_2\text{O}_3$ : $\text{Nb}_2\text{O}_5$  ( $\text{Bi}_3\text{Nb}_2\text{O}_7$ ) to 93:7  $\text{Bi}_2\text{O}_3$ : $\text{Nb}_2\text{O}_5$ . This region has received considerable attention as it forms a series of structurally complex, modulated superstructures [25–29] with variable and potentially useful dielectric properties [30,31]. Reported differences in the detailed phase relations in this region likely arise from kinetic effects, variations in synthesis (especially cooling methods), and/or differences in

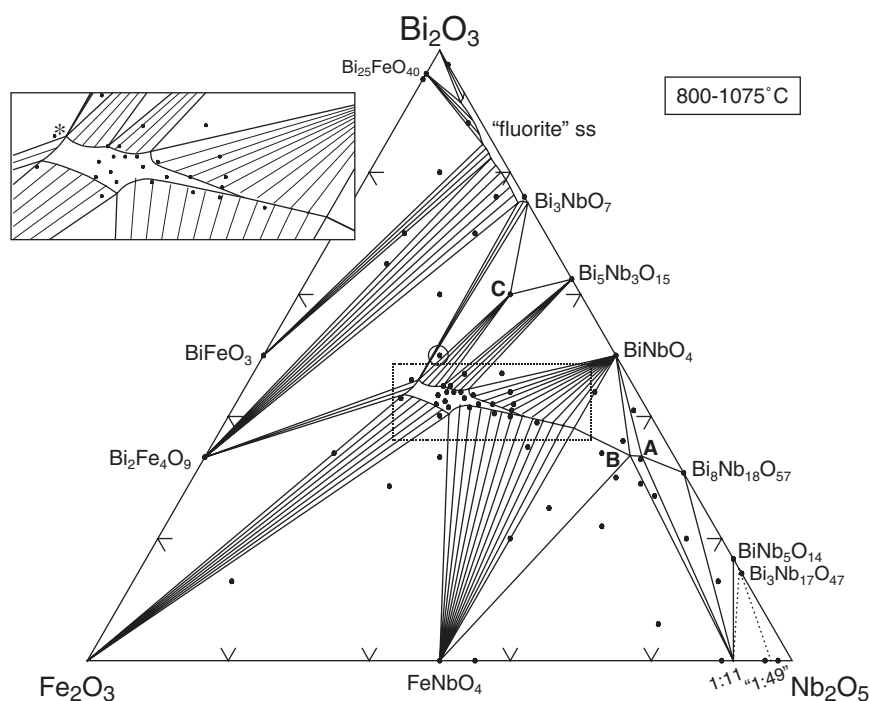


Fig. 1. Subsolidus phase equilibrium diagram in air for the  $\text{Bi}_2\text{O}_3$ : $\text{Fe}_2\text{O}_3$ : $\text{Nb}_2\text{O}_5$  system. Black dots denote the compositions of specimens prepared in the study; concentrations are on a molar fraction basis. A large, swordfish-shaped pyrochlore phase field forms near the center of the diagram (enlarged in the inset). Three other ternary phases were observed to form, apparently as point compounds: Compounds **A** and **B** are structurally related phases with approximate compositions  $\text{Bi}_{17}\text{Fe}_2\text{Nb}_{31}\text{O}_{106}$  and  $\text{Bi}_{17}\text{Fe}_3\text{Nb}_{30}\text{O}_{105}$ , respectively, and compound **C** is Aurivillius-type  $\text{Bi}_3\text{Fe}_{0.5}\text{Nb}_{1.5}\text{O}_9$ . The “pyrochlore-like” composition  $\text{Bi}_2\text{FeNbO}_7$  (open circle) falls considerably outside the pyrochlore field and corresponds to a three-phase mixture of  $\text{Bi}_3\text{NbO}_7$ , pyrochlore, and phase **C**. The limiting compositions of the pyrochlore field suggested by the present data are (inset: clockwise, beginning with the cusp marked with an asterisk)  $\text{Bi}_2\text{O}_3$ : $\text{Fe}_2\text{O}_3$ : $\text{Nb}_2\text{O}_5 = 0.460:0.300:0.240$  ( $\text{Bi}_{1.85}\text{Fe}_{1.21}\text{Nb}_{0.96}\text{O}_7$ ,  $a = 10.531(1)\text{Å}$ ),  $0.450:0.270:0.280$  ( $\text{Bi}_{1.77}\text{Fe}_{1.06}\text{Nb}_{1.01}\text{O}_7$ ,  $a = 10.516(1)\text{Å}$ ),  $0.445:0.235:0.320$  ( $\text{Bi}_{1.71}\text{Fe}_{0.90}\text{Nb}_{1.23}\text{O}_7$ ,  $a = 10.509(1)\text{Å}$ ),  $0.380:0.120:0.500$  ( $\text{Bi}_{1.33}\text{Fe}_{0.42}\text{Nb}_{1.75}\text{O}_7$ ,  $a = 10.504(1)\text{Å}$ ),  $0.405:0.285:0.310$  ( $\text{Bi}_{1.57}\text{Fe}_{1.10}\text{Nb}_{1.20}\text{O}_7$ ,  $a = 10.492(1)\text{Å}$ ), and  $0.436:0.334:0.230$  ( $\text{Bi}_{1.76}\text{Fe}_{1.35}\text{Nb}_{0.93}\text{O}_7$ ,  $a = 10.513(1)\text{Å}$ ).

characterization methods (e.g. X-ray or electron diffraction). For example, the present study, in agreement with early studies [24], did not find a sillenite-type compound at the composition  $\text{Bi}_{12}\text{Nb}_{0.29}\text{O}_{20-x}$  [26]. This specimen was a mixture of monoclinic  $\text{Bi}_2\text{O}_3$  and the fluorite-type solid solution after repeated heatings at 700 °C for a total of 414 h; however, a different heat treatment may have resulted in the metastable body-centered cubic form of  $\text{Bi}_2\text{O}_3$  (sillenite-type) [32] instead of the monoclinic polymorph.

In the ternary  $\text{Bi}_2\text{O}_3\text{:Fe}_2\text{O}_3\text{:Nb}_2\text{O}_5$  system four distinct ternary phases were observed to form (Fig. 1). Phases **A** and **B** occur near the stoichiometries  $\text{Bi}_{17}\text{Fe}_2\text{Nb}_{31}\text{O}_{106}$  and  $\text{Bi}_{17}\text{Fe}_3\text{Nb}_{30}\text{O}_{105}$ , respectively, and appear to have new structure types related to that of the binary phase  $\text{Bi}_8\text{Nb}_{18}\text{O}_{57}$ . Single crystals of these phases were obtained by slow-cooling off-stoichiometric melts, and the results of structural studies will be reported elsewhere. Phase **C** is  $\text{Bi}_3\text{Fe}_{0.5}\text{Nb}_{1.5}\text{O}_9$  and exhibits an Aurivillius-type structure similar to that of ferroelectric  $\text{Bi}_3\text{TiNbO}_9$  [33], further characterization of this phase will be described separately. The fourth ternary phase in this system is pyrochlore, which forms an extensive swordfish-shaped solid-solution region (Fig. 1, inset). During synthesis, the pyrochlore phase was kinetically dominant in partially reacted samples and was readily purified within the single-phase region, suggesting high thermodynamic stability. Numerous descriptions can be found for the pyrochlore crystal structure,  $^{\text{VIII}}\text{A}_2^{\text{VI}}\text{B}_2\text{O}_7$ , which is unusual in that it can be considered as two relatively independent interpenetrating networks, the first comprised of  $[\text{BO}_6]$  octahedra sharing all vertices, and the second consisting of  $[\text{O}'\text{A}_4]$  tetrahedra in an anti-cristobalite-type arrangement [34–36]. The structural formula is often written as  $(\text{A}_2\text{O}')(\text{B}_2\text{O}_6)$  or  $\text{A}_2\text{B}_2\text{O}_6\text{O}'$  to emphasize this interesting structural character. The larger *A*-cations are 8-fold (= 6 + 2) coordinated by six oxygens in puckered rings of the  $\text{B}_2\text{O}_6$  network plus two  $\text{O}'$  oxygens above and below in the  $\text{A}_2\text{O}'$  network. The structure inherently facilitates non-stoichiometry as the  $\text{A}_2\text{O}'$  network can be partially occupied, or in some cases completely absent; furthermore, numerous non-oxide and halide pyrochlores are known. In addition to extensive compositional ranges, pyrochlores exhibit a remarkable variety of exploitable physical properties hence the considerable technical importance of this class of solids [35,37–39].

$\text{Bi-Fe-Nb-O}$  pyrochlores have been previously reported to form at various stoichiometries including  $\text{Bi}_{1.34}\text{FeNbO}_6$  [40],  $\text{Bi}_2\text{FeNbO}_7$  [41–44],  $\text{Bi}_2\text{Fe}_2\text{Nb}_2\text{O}_{11}$  [45], and  $\text{Bi}_2\text{Fe}_2\text{NbO}_{8.5}$  [45]; however, under the conditions of the present study none of these are included in the single-phase field: composition  $\text{Bi}_{1.34}\text{FeNbO}_6$  falls in a two-phase field of pyrochlore plus a small amount of  $\text{Fe}_2\text{O}_3$ ; the “pyrochlore-like” composition  $\text{Bi}_2\text{FeNbO}_7$  forms a three-phase mixture as described in Fig. 1;  $\text{Bi}_2\text{Fe}_2\text{Nb}_2\text{O}_{11}$  formed a mixture of pyrochlore,  $\text{Fe}_2\text{O}_3$ , and  $\text{FeNbO}_4$ ; and composition  $\text{Bi}_2\text{Fe}_2\text{NbO}_{8.5}$  corresponds to a three-phase mixture of pyrochlore,  $\text{Fe}_2\text{O}_3$ , and  $\text{Bi}_2\text{Fe}_4\text{O}_9$ . As shown on the

diagram (Fig. 1),  $\text{Bi-Fe-Nb-O}$  pyrochlores form thermodynamically stable mixtures with the  $\text{Bi}_3\text{NbO}_7$  solid solution,  $\text{Bi}_3\text{Fe}_{0.5}\text{Nb}_{1.5}\text{O}_9$  (phase **C**),  $\text{Bi}_5\text{Nb}_3\text{O}_{15}$ ,  $\text{BiNbO}_4$ , phase **B**,  $\text{FeNbO}_4$ ,  $\text{Fe}_2\text{O}_3$ , and  $\text{Bi}_2\text{Fe}_4\text{O}_9$ . Compositions, nominal formulas, and refined unit cell parameters for single-phase  $\text{Bi-Fe-Nb-O}$  pyrochlores prepared in the present study are given in Table 1; all samples were brick-red in color. The trends observed in the unit cell parameters suggest that cell volume increases markedly with both Bi and vacancy concentration.

Observed, indexed X-ray powder diffraction data for the pyrochlore 0.4400:0.2700:0.2900  $\text{Bi}_2\text{O}_3\text{:Fe}_2\text{O}_3\text{:Nb}_2\text{O}_5$  are given in Table 2. As noted previously [35], the 442 reflection, forbidden for an ideal pyrochlore structure, was easily observed in this pattern and in all patterns of pyrochlore and pyrochlore-containing specimens prepared in this study. The 442 reflection was also readily observed in precession photos of single crystals. Similar to the  $\text{Bi-Zn-Nb-O}$  pyrochlores [35,46], the non-zero intensity of this diagnostic reflection indicates the presence of displacements off ideal crystallographic sites. The consistent observation of this reflection indicates that all  $\text{Bi-Fe-Nb-O}$  pyrochlores exhibit structural displacements. Furthermore, the stoichiometric location of the pyrochlore phase field, as also found for the analogous  $\text{Bi-M-Nb-O}$  systems ( $M = \text{Zn}$  [35],  $\text{Mn}$  [47], or  $\text{Co}$  [48]), occurs at substantially lower Bi concentrations than conventional formulations placing only Bi on the *A*-sites and the smaller *M/Nb* cations on the *B*-sites. The pyrochlore field includes compositions with “excess” *B*-cations that require mixing of some Fe on the *A*-sites with  $\text{Bi}^{3+}$ , as found for Zn in all  $\text{Bi-Zn-Nb-O}$  pyrochlores [35]. The limiting compositions observed for the pyrochlore field (Fig. 1) suggest that the  $\text{Fe}^{3+}$  concentration on the *A*-sites can range from  $\approx 4\%$  to

Table 1

Compositions, nominal formulas, and unit cell parameters (*a*, space group  $Fd\bar{3}m$ , #227) for single-phase pyrochlore specimens prepared in this study

$\text{Bi}_2\text{O}_3\text{:Fe}_2\text{O}_3\text{:Nb}_2\text{O}_5$	Nominal formula	<i>a</i> , Å
0.4500:0.2700:0.2800	$\text{Bi}_{1.770}\square_{0.067}\text{Fe}_{1.062}\text{Nb}_{1.101}\text{O}_7$	10.516(1)
0.4400:0.2700:0.2900	$\text{Bi}_{1.721}\square_{0.089}\text{Fe}_{1.056}\text{Nb}_{1.134}\text{O}_7$	10.508(1)
0.4350:0.2850:0.2800	$\text{Bi}_{1.711}\square_{0.067}\text{Fe}_{1.121}\text{Nb}_{1.101}\text{O}_7$	10.503(1)
0.4400:0.2600:0.3000	$\text{Bi}_{1.711}\square_{0.111}\text{Fe}_{1.011}\text{Nb}_{1.167}\text{O}_7$	10.510(1)
0.4400:0.2500:0.3100	$\text{Bi}_{1.702}\square_{0.133}\text{Fe}_{0.9668}\text{Nb}_{1.199}\text{O}_7$	10.510(1)
0.4250:0.2800:0.2950	$\text{Bi}_{1.657}\square_{0.100}\text{Fe}_{1.092}\text{Nb}_{1.150}\text{O}_7$	10.490(1)
0.4300:0.2500:0.3200	$\text{Bi}_{1.654}\square_{0.154}\text{Fe}_{0.9615}\text{Nb}_{1.231}\text{O}_7$	10.504(1)
0.4200:0.2950:0.2850	$\text{Bi}_{1.647}\square_{0.078}\text{Fe}_{1.157}\text{Nb}_{1.118}\text{O}_7$	10.495(1)
0.4150:0.2800:0.3050	$\text{Bi}_{1.609}\square_{0.122}\text{Fe}_{1.086}\text{Nb}_{1.183}\text{O}_7$	10.494(1)
0.4200:0.2350:0.3450	$\text{Bi}_{1.593}\square_{0.206}\text{Fe}_{0.8916}\text{Nb}_{1.309}\text{O}_7$	10.501(1)
0.4200:0.2150:0.3650	$\text{Bi}_{1.576}\square_{0.246}\text{Fe}_{0.8070}\text{Nb}_{1.370}\text{O}_7$	10.501(1)

These compositions correspond to the points within the six-sided pyrochlore region shown in Fig. 1. For purposes of comparison, the formulas have been normalized to seven oxygens (full occupancy of the  $\text{O}'$  site) and assume  $\text{Fe}^{3+}$ ; therefore, the number of resulting *A*-site vacancies ( $\square$ ) correspond to minima. Although the metal ratios given here are precise, the actual populations on the *A* and *B* sites depend on the  $\text{O}'$  occupancy factors, which are uncertain.

Table 2

Observed X-ray powder diffraction data for the pyrochlore  $\text{Bi}_2\text{O}_3:\text{Fe}_2\text{O}_3:\text{Nb}_2\text{O}_5 = 0.4400:0.2700:0.2900$  ( $\text{Bi}_{1.721}\text{Fe}_{1.056}\text{Nb}_{1.134}\text{O}_7$ ), space group  $Fd\bar{3}m$  (no. 227),  $a = 10.508(1)$  Å

<i>h</i>	<i>k</i>	<i>l</i>	$2\theta_{\text{obs}}$	$I_{\text{obs}}$	$2\theta_{\text{calc}}$	$\Delta 2\theta$	$d_{\text{obs}}$
1	1	1	14.615	7	14.589	-0.026	6.0559
2	2	0	23.914	<1	23.933	0.019	3.7180
3	1	1	28.146	8	28.143	-0.003	3.1679
2	2	2	29.420	100	29.422	0.002	3.0335
4	0	0	34.101	36	34.102	0.002	2.6271
3	3	1	37.271	11	37.270	-0.001	2.4106
4	2	2	42.088	<1	42.093	0.005	2.1452
3	3	3	44.776	3	44.780	0.004	2.0224
4	4	0	49.000	51	48.999	-0.001	1.8575
5	3	1	51.400	3	51.403	0.003	1.7763
4	4	2	52.179	<1	52.187	0.008	1.7516
6	2	0	55.234	1	55.243	0.009	1.6617
5	3	3	57.451	<1	57.462	0.012	1.6027
6	2	2	58.192	42	58.190	-0.002	1.5841
4	4	4	61.044	11	61.045	0.001	1.5167
7	1	1	63.124	1	63.136	0.012	1.4717
6	4	2	66.540	<1	66.538	-0.002	1.4041
5	5	3	68.541	<1	68.538	-0.004	1.3680

15%.<sup>4</sup> These concentrations are considerably lower than those for the analogous Bi–M–Nb–O pyrochlores with  $M = \text{Zn}$  ( $\approx 16$ –26%) [35],  $\text{Mn}$  ( $\approx 12$ –27%) [47], or  $\text{Co}$  ( $\approx 8$ –25%) [48], and may be related to the occurrence of the larger divalent  $\text{Zn}^{2+}$ ,  $\text{Mn}^{2+}$ , and  $\text{Co}^{2+}$  cations in those systems. Variations in the locations of the pyrochlore fields in these systems also suggest different tolerance levels for *A*-site vacancy concentrations. For example, the shape of the pyrochlore field reported here is extremely wide in Fe/Nb variability ( $>0.20$  mole fraction) compared to the analogous Zn, Mn, and Co systems, suggesting that the Fe pyrochlore accepts considerably higher levels of *A*-site vacancies. Such appreciable chemical differences in the  $A_2O'$  networks may drive variations in the detailed displacive behavior in these pyrochlores, both within a chemical system and from system to system; e.g. Withers et al. [36] have recently reported an electron diffraction study of a Bi–Fe–Nb–O pyrochlore which concludes that the displacements in the  $A_2O'$  network differ from those in the Bi–Zn–Nb–O analog [46].

### 3.2. Oxidation state of Fe in pyrochlore

The valence state of Fe in a single-phase pyrochlore sample of composition 0.4400:0.2700:0.2900  $\text{Bi}_2\text{O}_3:\text{Fe}_2\text{O}_3:\text{Nb}_2\text{O}_5$  was inferred from analyses of Fe- $L_{2,3}$  ELNES. The  $L_3$  and  $L_2$  edges observed for the pyrochlore sample and the reference compounds  $\text{Fe}_2\text{O}_3$  ( $\text{Fe}^{3+}$ ) and  $\text{FeTiO}_3$  ( $\text{Fe}^{2+}$ ) are shown in Fig. 2. For transition metals

<sup>4</sup>Calculated by assuming  $\text{Fe}^{3+}$  and full occupancy of the  $O'$  site, which results in maximum estimates for  $\text{Fe}^{3+}$   $A$ -site concentrations and minimum estimates for  $A$ -site vacancy concentrations.

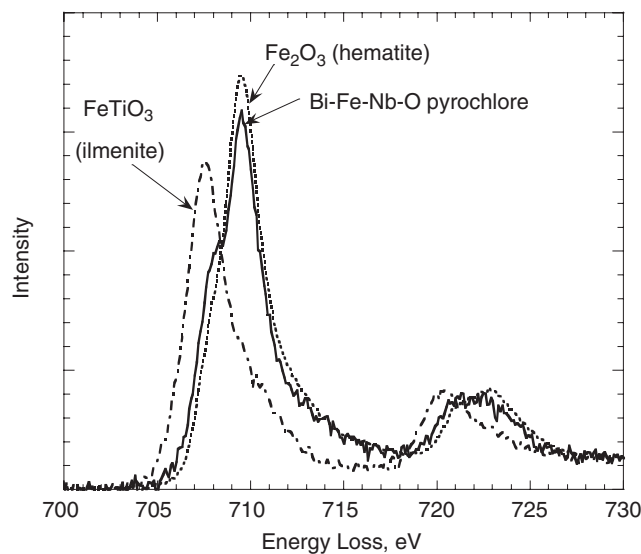


Fig. 2. EELS spectra showing the Fe- $L_{2,3}$  edge for the pyrochlore  $\text{Bi}_{1.721}\text{Fe}_{1.056}\text{Nb}_{1.134}\text{O}_7$  (0.4400:0.2700:0.2900  $\text{Bi}_2\text{O}_3:\text{Fe}_2\text{O}_3:\text{Nb}_2\text{O}_5$ ),  $\text{Fe}_2\text{O}_3$  (hematite), and  $\text{FeTiO}_3$  (ilmenite) samples. The data suggest the presence of some  $\text{Fe}^{2+}$  in the pyrochlore sample; however, up to 18% of the Fe in the pyrochlore sample may be located in non-octahedrally coordinated sites, thus modifying the  $L_{2,3}$  intensities.

with partially occupied  $3d$  states, these so-called “white” lines arise from  $2p^{3/2} \rightarrow 3d^{5/2}3d^{5/2}$  and  $2p^{1/2} \rightarrow 3d^{3/2}$  transitions, and their intensities reflect the densities of unoccupied states in the  $3d$  bands [49]. Systematic EELS studies have established a clear correlation between the white line intensities and the valence state of the  $3d$  transition metals [50,51]. The excitation of the  $2p$  electrons is highly localized so that the resulting spectra represent a linear combination of the contributions from all absorbing atoms, thus enabling a determination of the relative proportions of the different oxidation states in mixed-valence compounds. In the present work the method of Garvie and Buseck [52] was used to estimate the  $\text{Fe}^{3+}/\Sigma\text{Fe}$  ratio in the pyrochlore sample by fitting the observed Fe- $L_{2,3}$  spectrum with a linear combination of those obtained for  $\text{Fe}_2\text{O}_3$  and  $\text{FeTiO}_3$  (in both reference compounds Fe is octahedrally coordinated by oxygen). Prior to fitting, the reference spectra were normalized by the continuum intensity above the  $L_{2,3}$  lines (740–780 eV). The  $L_3$  and  $L_2$  intensities were separated from the continuum by subtracting a straight line fitted between 705 and 730 eV. These analyses yielded  $\text{Fe}^{3+}/\Sigma\text{Fe} \approx 0.8$  for the pyrochlore 0.4400:0.2700:0.2900  $\text{Bi}_2\text{O}_3:\text{Fe}_2\text{O}_3:\text{Nb}_2\text{O}_5$  which suggests the presence of  $\text{Fe}^{2+}$ ; however, the validity of this result is affected by the location of up to 18% of the Fe cations in the  $A_2O'$  network, in non-octahedral coordination sites. The brick red color of the Bi–Fe–Nb–O pyrochlores suggests that Fe is entirely present as the trivalent ion. Likely, the small differences observed in the intensities of the  $L_{3,2}$  lines for  $\text{Fe}_2\text{O}_3$  and the pyrochlore sample are caused by non-octahedral coordination of the *A*-site Fe cations.

### 3.3. Structural refinement of the pyrochlore phase

The highly symmetrical ideal pyrochlore structure  $A_2B_2O_6O'$  crystallizes in space group  $Fd\bar{3}m$  with  $A$  and  $B$  cations on two special positions (16*d*, 16*c*) and oxygens on two sites, 48*f* (O) and 8*b* (O'), which result in a single positional variable ( $x$  for the 48*f* site oxygen in the  $B_2O_6$  octahedral network). As expected, this model resulted in anomalously large thermal parameters for the  $A$ -site cations and the O' oxygens in an initial structural refinement of the pyrochlore  $\text{Bi}_2\text{O}_3:\text{Fe}_2\text{O}_3:\text{Nb}_2\text{O}_5 = 0.4400:0.2700:0.2900$  using neutron powder diffraction data. Various models have been used to refine the structures of pyrochlores in which the  $A_2O'$  network is displaced from ideal positions. For  $\text{Tl}_2\text{TA}_2\text{O}_6$ ,  $\text{Tl}^+$  ions were displaced from the 16*d* to the 32*e* sites, yielding two equivalent half-occupied positions [53]. A later study of  $\text{Tl}_2\text{Nb}_2\text{O}_{6+x}$  phases concluded that, in agreement with NMR results, the forbidden reflections were better accounted for by anisotropic thermal (dynamic rather than static) displacements [54]. For  $\text{Bi}_{2-y}\text{Ru}_2\text{O}_{7-z}$  [55],  $\text{Bi}_{2-y}\text{Yb}_y\text{Ru}_2\text{O}_{7-z}$  [56], and  $\text{Bi}_{2-x}\text{CrTaO}_{7-y}$  [57], Bi was displaced to the 96*h* site, yielding a toroid of six possible equivalent positions. In the structural refinement of  $\text{Bi}_{1.5}\text{Zn}_{0.92}\text{Nb}_{1.5}\text{O}_{6.92}$  [46] both the  $A$  cations and O' oxygens were displaced to 96*g* sites, resulting in six equivalent possible positions for the former and 12 for the latter; a study of short-range ordering has also been

reported for this pyrochlore [58]. For  $\text{Bi}_{2-y}\text{Ru}_2\text{O}_{7-z}$  [55], the O' oxygens were displaced from the 8*b* to the 32*e* site, distributed among four equivalent positions. Although the displaced sites in the different models are crystallographically distinct, the refinements in general indicate similar magnitudes for the displacements of  $A$  and O' from the ideal positions (on the order of  $\leq 0.5 \text{ \AA}$ ).

Rietveld refinement results obtained for pyrochlore-type 0.4400:0.2700:0.2900  $\text{Bi}_2\text{O}_3:\text{Fe}_2\text{O}_3:\text{Nb}_2\text{O}_5$  using six different models are given in Table 3. Cation occupancies were fixed according to the preparative analytical masses; no impurity phases were detectable by X-ray or neutron diffraction. An oxidation state of 3+ was assumed for Fe and all  $\text{Nb}^{5+}$  was placed on the  $B$ -sites, which were then completely filled with  $\text{Fe}^{3+}$ ; the remaining  $\text{Fe}^{3+}$  was placed on the  $A$ -sites with  $\text{Bi}^{3+}$ , and the O' sites were assumed to be completely filled. Model 1 corresponds to the ideal pyrochlore structure; the anomalously large thermal parameters obtained for the  $A$  and O' sites, combined with the observation of 442-type reflections in the powder diffraction patterns, confirm the presence of positional displacements. In Models 2 and 3 the  $A$ -site cations were displaced to the 96*h* and 96*g* sites, respectively. Each substantially improved the fit and reduced the  $A$ -site thermal parameter. Models 4 and 5 retain the  $A$ -site cations on 96*g* sites and displace O' to 32*e* and 96*g* sites, respectively. As seen in Table 3, the fit statistics obtained for Models 3, 4 and 5 are similar but Model 4 returns a

Table 3

Refined structural parameters for pyrochlore-type 0.4400:0.2700:0.2900  $\text{Bi}_2\text{O}_3:\text{Fe}_2\text{O}_3:\text{Nb}_2\text{O}_5$  at 10 K using neutron powder diffraction data, space group  $Fdm$  (no. 227)

	Model 1	Model 2	Model 3	Model 4	Model 5	Model 6
$a$ (Å)	10.50380(12)	10.50368(6)	10.50366(6)	10.50366(6)	10.50366(6)	10.50368(6)
$A$ -site	16 <i>d</i>	96 <i>h</i>	96 <i>g</i>	96 <i>g</i>	96 <i>g</i>	96 <i>h</i>
Occ. (Bi/Fe)	0.860/0.095	0.143/0.016	0.143/0.016	0.143/0.016	0.143/0.016	0.143/0.016
$x$	1/2	0	0.4651(3)	0.4652(3)	0.4652(3)	0
$y$	1/2	0.22129(8)	0.5148(3)	0.5149(3)	0.5149(3)	0.22133(8)
$z$	1/2	0.77871(8)	0.5148(3)	0.5149(3)	0.5149(3)	0.77867(8)
$U_{\text{iso}}$ (Å <sup>2</sup> ) × 100	10.55(13)	1.69(5)	1.57(5)	1.60(5)	1.59(5)	1.73(5)
$B$ -site	16 <i>c</i>	16 <i>c</i>	16 <i>c</i>	16 <i>c</i>	16 <i>c</i>	16 <i>c</i>
Occ. (Fe/Nb)	0.433/0.567	0.433/0.567	0.433/0.567	0.433/0.567	0.433/0.567	0.433/0.567
$U_{\text{iso}}$ (Å <sup>2</sup> ) × 100	0.93(3)	0.84(2)	0.82(2)	0.82(2)	0.82(2)	0.83(2)
O-site	48 <i>f</i>	48 <i>f</i>	48 <i>f</i>	48 <i>f</i>	48 <i>f</i>	48 <i>f</i>
Occ. (O)	1	1	1	1	1	1
$x$	0.31952(12)	0.31972(6)	0.31971(6)	0.31968(6)	0.31968(6)	0.31966(6)
$U_{\text{iso}}$ (Å <sup>2</sup> ) × 100	1.56(3)	1.320(14)	1.30(1)	1.30(1)	1.29(1)	1.31(1)
O'-site	8 <i>b</i>	8 <i>b</i>	8 <i>b</i>	32 <i>e</i>	96 <i>g</i>	32 <i>e</i>
Occ. (O)	1	1	1	1/4	0.0833	1/4
$x$	3/8	3/8	3/8	0.3632(1)	0.359(5)	0.3601(6)
$y$	3/8	3/8	3/8	0.3632(1)	0.359(5)	0.3601(6)
$z$	3/8	3/8	3/8	0.3632(1)	0.370(5)	0.3601(6)
$U_{\text{iso}}$ (Å <sup>2</sup> ) × 100	7.5(2)	7.5(1)	7.5(1)	5.9(4)	5(1)	4.7(3)
$R_{\text{wp}}$ (%)	9.70	4.97	4.90	4.90	4.90	4.95
$R_{\text{p}}$ (%)	6.70	3.99	3.98	3.96	3.96	3.98
$\chi^2$	7.00	1.84	1.79	1.79	1.79	1.83

Atoms retained on special positions in all models are B-site Fe,Nb on 16*c* (0, 0, 0) and O at ( $x$ , 0, 0).

better thermal parameter for  $O'$ —lower than that obtained with Model 3 and with less uncertainty than Model 5. Model 6, which keeps  $O'$  on the  $32e$  site as for Model 4, but displaces  $A$ -cations to  $96h$  instead of  $96g$  sites, resulted in a lower thermal parameter for  $O'$  but slightly worse fit statistics. Models 4 and 6 are very similar and differ only in the orientation of the toroid of six possible positions for the  $A$ -cations. The differences in the refinements suggest that it may not be possible to distinguish between these two models; however, displacements of the  $A_2O'$  network off ideal sites is clearly confirmed. As seen in Table 3, neither Model 4 nor Model 6 reduced the  $O'$  thermal parameter below  $\sim 5 \times 10^{-2} \text{ \AA}^2$ , in contrast to the refinement [46] of  $\text{Bi}_{1.5}\text{Zn}_{0.92}\text{Nb}_{1.5}\text{O}_{6.92}$  which used Model 5. This may be related to significantly different concentrations of smaller  $B$ -type cations on the  $A$ -sites: whereas in  $\text{Bi}_{1.5}\text{Zn}_{0.92}\text{Nb}_{1.5}\text{O}_{6.92}$  more than 20% of the  $A$ -sites are occupied by Zn, in the Fe pyrochlore refined here the concentration is less than 10%, which should reduce the driving force for  $O'$  displacements as well as correlations between  $O'$  displacements and  $A$ -site occupancy. The large  $O'$  thermal parameter obtained for the Bi–Fe–Nb–O pyrochlore may also indicate the coexistence of different displacive arrangements.

Final refinement results at 10 and 293 K using Model 4 are given in Table 4; the difference profiles are shown in Fig. 3. The similar results obtained at the two temperatures suggest that the displacements are static in nature. The displacively disordered structure is illustrated in Fig. 4 [59]. The refined  $O'$  occupancy at 10 K (the difference from that obtained at 293 K is not considered statistically significant) is within one e.s.d. of 0.250, suggesting very few, if any,  $O'$  vacancies. With full occupancy of the  $O'$  site and trivalent Fe, the structural formula for the pyrochlore phase is  $\text{Bi}_{1.721}\text{Fe}_{0.190}(\text{Fe}_{0.866}\text{Nb}_{1.134})\text{O}_7$ . The  $[(\text{Fe},\text{Nb})\text{O}_6]$  octahedra in the  $B_2\text{O}_6$  network are nearly regular, with metal–oxygen distances of  $1.997 \text{ \AA}$  ( $\times 6$ ), and  $\text{O–B–O}$  angles deviating about  $2.9^\circ$  from  $90^\circ$ . The observed bond valence sum of 4.06 v.u. for the  $B$  site, calculated using the  $R_o$  parameters for  $\text{Nb}^{5+}$  and  $\text{Fe}^{3+}$  [60] and the occupancies in Table 4,

agrees well with the value of 4.13 v.u. expected from the formal valences. The  $A$ -site cations and neighboring  $O'$  positions are both displacively disordered, therefore calculation of bond valence sums is less meaningful. However, the positional displacements result in a number of considerably shorter  $A\text{–O}$  and  $A\text{–O}'$  distances compared to the ideal structure (Model 1): Observed  $A$ -site distances to the framework oxygens ( $A\text{–O}$ ) are 2.232, 2.469 ( $\times 2$ ), 2.888 ( $\times 2$ ), and 3.074  $\text{ \AA}$  (compared to 2.652  $\text{ \AA}$  ( $\times 6$ ) in the ideal structure), and observed  $A\text{–O}'$  distances range from 2.026 to 2.470  $\text{ \AA}$  (compared to 2.275  $\text{ \AA}$  ( $\times 2$ ) in the ideal structure). The shorter distances available in the displaced structure can reasonably accommodate the smaller  $\text{Fe}^{3+}$  and can also improve the bonding for  $\text{Bi}^{3+}$  (which would have an undersaturated bond valence sum of 2.55 v.u. in the ideal structure).

The anisotropic thermal parameters for the oxygens were also refined in the final stages of the neutron diffraction study (Table 4) and indicated that the  $O'$  displacements are strongly anisotropic. The probability density distribution obtained for  $O'$  is represented in Fig. 5 by the four

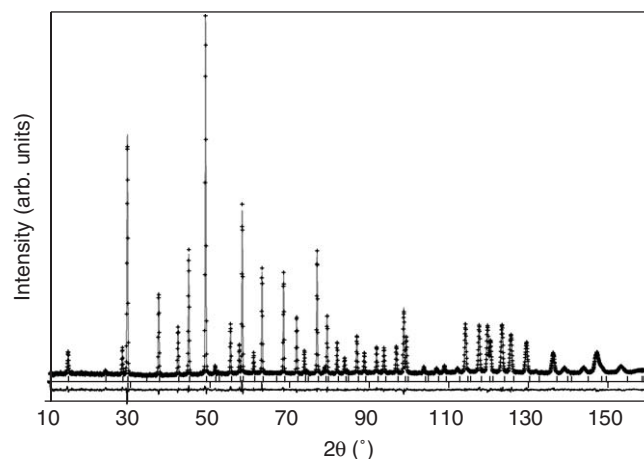


Fig. 3. Observed, calculated, and difference neutron diffraction profiles for the pyrochlore 0.4400:0.2700:0.2900  $\text{Bi}_2\text{O}_3\text{:Fe}_2\text{O}_3\text{:Nb}_2\text{O}_5$  at 10 K. Tick marks indicate allowed reflection positions.

Table 4

Final Rietveld refinement results for pyrochlore-type 0.4400:0.2700:0.2900  $\text{Bi}_2\text{O}_3\text{:Fe}_2\text{O}_3\text{:Nb}_2\text{O}_5$  using Model 4 (space group  $Fd\bar{3}m$ , #227) and neutron powder diffraction data

	Site	$x$	$y$	$z$	$U_{\text{iso}} (\text{ \AA}^2) \times 100$	Occ.
Bi/Fe	96g	0.4666(3)	0.5164(3)	0.5164(3)	1.67(4)	0.1434/0.01583
		0.4659(3)	0.5141(3)	0.5141(3)	2.22(6)	
Nb/Fe	16c	0	0	0	0.90(1)	0.5670/0.4330
		0	0	0	1.20(2)	
O	48f	0.31986(5)	0.125	0.125	1.40 <sup>a</sup>	1
		0.31992(7)	0.125	0.125	1.87(2)	
$O'$	32e	0.3919(4)	0.3919(4)	0.3919(4)	4.4(2)	0.243(2)
		0.3625(11)	0.3625(11)	0.3625(11)	4.9(4)	

The upper and lower entries correspond to 10 K and 293 K, respectively. The lattice parameter, cell volume, and final fit statistics at 10 K (293 K) are  $a = 10.50364(5) \text{ \AA}$  ( $10.51037(5) \text{ \AA}$ ), volume =  $1158.83(2) \text{ \AA}^3$  ( $1161.06(1) \text{ \AA}^3$ ),  $R_{\text{wp}} = 4.11\%$  ( $5.02\%$ ),  $R_{\text{p}} = 3.36\%$  ( $4.06\%$ ),  $R(F^2) = 2.58\%$  ( $4.61\%$ ),  $\chi^2 = 1.26$  (1.67). Neglecting  $O'$  vacancies the formula is  $\text{Bi}_{1.721}\text{Fe}_{1.056}\text{Nb}_{1.134}\text{O}_7$ .

<sup>a</sup>  $U_{11} = 0.0179(3) \text{ \AA}^2$ ,  $U_{22} = U_{33} = 0.0120(2) \text{ \AA}^2$ ,  $U_{12} = U_{13} = 0$ ,  $U_{23} = 0.0069(2) \text{ \AA}^2$ .

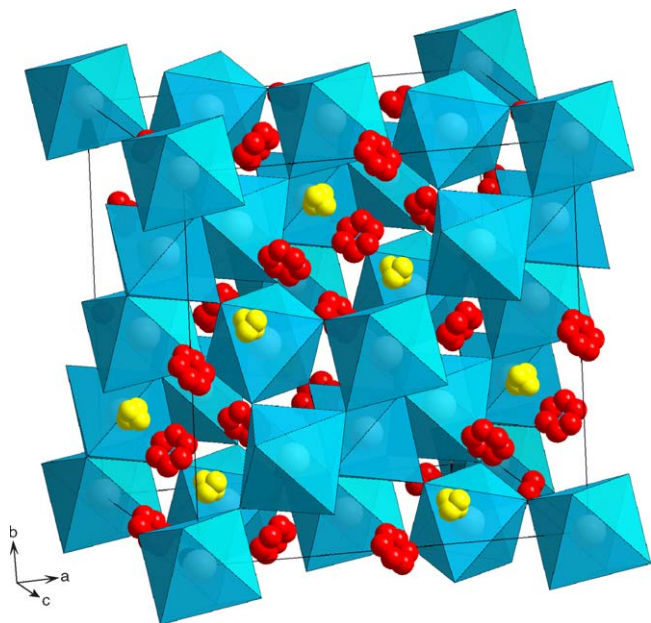


Fig. 4. Crystal structure of the displacively disordered pyrochlore 0.4400:0.2700:0.2900  $\text{Bi}_2\text{O}_3:\text{Fe}_2\text{O}_3:\text{Nb}_2\text{O}_5$  ( $\text{Bi}_{1.721}\text{Fe}_{0.190}(\text{Fe}_{0.866}\text{Nb}_{1.134})\text{O}_7$ ) according to the Rietveld refinement results (10 K) given in Table 4. The vertex-linked polyhedra represent the octahedral  $B_2O_6 = (\text{Fe},\text{Nb})_2O_6$  network. The toroids of lighter (red) spheres represent the six equivalent 96g positions for the *A*-site Bi/Fe cations, and the tetrahedral clusters of darker (yellow) spheres denote the four equivalent 32e sites for the displaced  $O'$  oxygens. The final refinement results indicate that the *A*-site cations are displaced 0.43 Å from the ideal 16d position, while  $O'$  is displaced 0.29 Å from the high-symmetry 8b position.

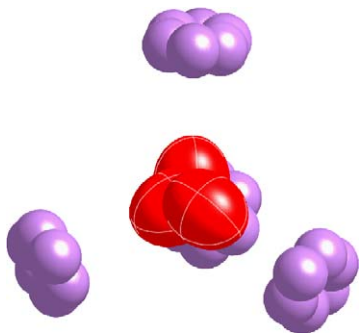


Fig. 5. Detailed view of one  $[O'(\text{Bi},\text{Fe})_4]$  group in the displaced  $A_2O'$  network of the pyrochlore  $\text{Bi}_{1.721}\text{Fe}_{1.056}\text{Nb}_{1.134}\text{O}_7$  (Table 4, 10 K). The four toroids of lighter (purple) spheres represent the 96g positions for the *A*-site Bi/Fe cations. The anisotropic thermal parameters for  $O'$  (100% probability) are represented by the four darker (red) ellipsoids (32e sites) elongated preferentially along the  $\langle 111 \rangle$  directions. The centers of the ellipsoids are displaced  $\sim 0.29$  Å from the ideal 8b position, but a large probability density is observed at the 8b site where the four ellipsoids overlap.

ellipsoids elongated preferentially along the  $\langle 111 \rangle$  directions. The centers of the individual ellipsoids are displaced by  $\sim 0.29$  Å toward the ideal *A*-sites; nevertheless, a large probability density is observed at the ideal  $O'$  8b positions where the four ellipsoids overlap. This anisotropic distribution cannot be described using a single Wyckoff position with a small isotropic displacement parameter.

These displacements of  $O'$  atoms appear to be similar to those reported for  $\text{Bi}_2\text{Ti}_2\text{O}_7$  [61], which were described using a combination of 8b and 32e sites with isotropic displacement parameters—such a combination provides the closest approximation to the anisotropic  $O'$  displacements shown in Fig. 5. In  $\text{Bi}_2\text{Ti}_2\text{O}_7$ , 100% of the  $[A_4O']$  configurations are  $[\text{Bi}_4O']$ , which is also nearly the case for the Bi–Fe–Nb–O pyrochlore since the concentration of Fe on the *A*-sites is less than 10%. Therefore, the  $O'$  displacements in both cases are driven primarily by Bi displacements, which modify the regularity of the  $[\text{Bi}_4O']$  tetrahedra so that, for many local configurations, the  $O'$  atoms remain on their ideal sites. The behavior of  $O'$  in the Bi–Fe–Nb–O compound is very different from that encountered in the Bi–Zn–Nb–O pyrochlore which contains a substantial fraction of Zn (up to 25%) on the *A*-sites and presumably exhibits a preference for local  $[\text{Bi}_3\text{Zn}]$  configurations [58]. In that case, the  $O'$  atoms are pulled preferentially toward the strongly under-bonded *A*-site Zn cations thus yielding a spherical shell-like distribution for the  $O'$  probability density with a zero density on the ideal 8b sites [46]. The displacements of the *A* cations from the ideal sites are similar in the Fe (0.43 Å) and Zn (0.39 Å) pyrochlores; however, the  $O'$  displacements from the 8b position are considerably smaller in the Fe system (0.29 Å compared to 0.46 Å in the Zn system). Therefore, in the Bi–Fe–Nb–O pyrochlore the displacive disorder manifests predominantly as rotations of the  $[O'A_4]$  tetrahedra [36], whereas in the Bi–Zn–Nb–O analog similar rotations are accompanied by marked displacements of the central  $O'$  atoms.

### 3.4. Magnetic properties of pyrochlore phases

Magnetic data obtained for five different single-phase Bi–Fe–Nb–O pyrochlore samples indicated qualitatively similar properties. The field dependence of the magnetization confirmed that all samples were overall paramagnetic in nature. The temperature dependence of the magnetic susceptibility, and its inverse, for the pyrochlore with composition 0.4400:0.2700:0.2900  $\text{Bi}_2\text{O}_3:\text{Fe}_2\text{O}_3:\text{Nb}_2\text{O}_5$  are shown in Fig. 6. The inverse susceptibility vs. temperature data show upward curvature at the lowest temperatures and at high temperatures deviate somewhat from linear Curie–Weiss behavior. For all five pyrochlores, approximate Curie–Weiss fits to the most linear regions between  $\sim 150$  and 300 K extrapolated to large negative temperature intercepts (Table 5) indicative of appreciable antiferromagnetic cooperative interactions. In addition, all of the observed effective magnetic moments suggested by the slopes of the Curie–Weiss fits (Table 5) are depressed relative to the spin-only values expected for  $\text{Fe}^{3+}$  ( $3d^5$ , high spin  $S = 5/2$ ). The slight curvature observed in the magnetization vs. field data at 4.2 K (Fig. 5, inset) suggests the presence of some superparamagnetic effects. The complex magnetic behavior exhibited by the Bi–Fe–Nb–O pyrochlores is not surprising given the triangular symmetry

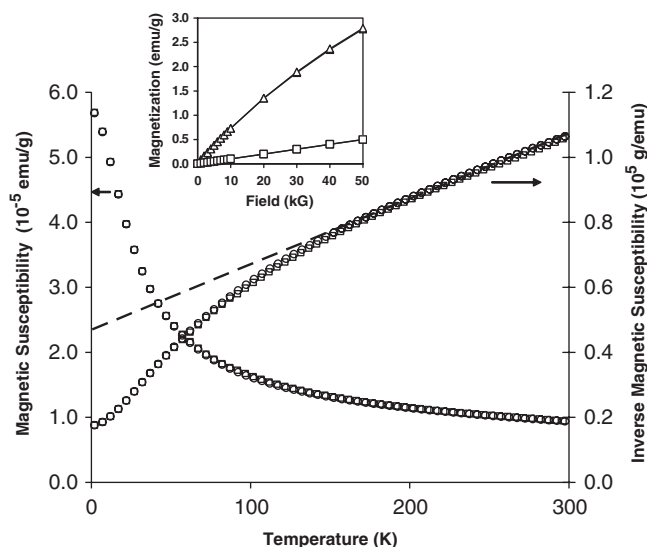


Fig. 6. Temperature dependence of the zero-field-cooled (circles) and field-cooled (squares) mass susceptibility and inverse mass susceptibility for the pyrochlore 0.4400:0.2700:0.2900  $\text{Bi}_2\text{O}_3\text{:Fe}_2\text{O}_3\text{:Nb}_2\text{O}_5$  at an applied field of 50 kG. Similar results were obtained with an applied field of 20 kG. The inset shows the field dependence of the magnetization measured at 4.2 K (triangles) and 300 K (squares). (Lines are present to guide the eye.) The slight curvature observed in the 4.2 K data suggests the presence of weak superparamagnetic effects. (Units: To convert susceptibility values in  $\text{emu/g}$  to SI units  $\text{m}^3/\text{kg}$ , multiply by  $4\pi/10^3$ . To convert field values in Oe (or G) to SI units  $\text{A/m}$ , multiply by  $10^3/4\pi$ . Magnetization values in  $\text{emu/g}$  units are numerically equal to SI units of  $\text{A m}^2/\text{kg}$  [62]).

Table 5

Magnetic data for single-phase Bi–Fe–Nb–O pyrochlore specimens; formulas assume  $\text{Fe}^{3+}$  and are normalized to seven oxygens for convenience. The effective moments ( $\mu_{\text{eff}}/\text{mol Fe}$ ) and temperature-axis intercepts ( $\theta$ , K) were approximated from linear fits of the inverse susceptibility data above  $\sim 150$  K. The observed moments  $\mu_{\text{eff}}$  are lower than the calculated spin-only value for high-spin  $3d^5 \text{Fe}^{3+}$  ( $5.92 \mu_B$ )

$\text{Bi}_2\text{O}_3\text{:Fe}_2\text{O}_3\text{:Nb}_2\text{O}_5$	Nominal formula	$\mu_{\text{eff}}/\text{mol Fe}$ ( $\mu_B$ )	$\theta$ (K)
0.4400:0.2700:0.2900	$\text{Bi}_{1.721}\text{Fe}_{1.056}\text{Nb}_{1.134}\text{O}_7$	4.87	–233
0.4350:0.2850:0.2800	$\text{Bi}_{1.711}\text{Fe}_{1.121}\text{Nb}_{1.101}\text{O}_7$	4.91	–278
0.4250:0.2800:0.2950	$\text{Bi}_{1.657}\text{Fe}_{1.092}\text{Nb}_{1.150}\text{O}_7$	5.21	–240
0.4200:0.2950:0.2850	$\text{Bi}_{1.647}\text{Fe}_{1.157}\text{Nb}_{1.118}\text{O}_7$	5.23	–273
0.4200:0.2150:0.3650	$\text{Bi}_{1.576}\text{Fe}_{0.8070}\text{Nb}_{1.370}\text{O}_7$	4.84	–164

of the metal lattices which results in magnetic frustration [63]. Pyrochlore compounds are known to exhibit a wide range of cooperative magnetic properties and, for example, are of significant interest as ‘spin-ice’ systems [64,65].

### 3.5. Dielectric properties of the pyrochlore phase

The relative permittivity (corrected for 6% porosity) and dielectric loss as a function of temperature and frequency for the single-phase pyrochlore 0.4250:0.2800:0.2950  $\text{Bi}_2\text{O}_3\text{:Fe}_2\text{O}_3\text{:Nb}_2\text{O}_5$  ( $\text{Bi}_{1.657}\text{Fe}_{1.092}\text{Nb}_{1.150}\text{O}_7$ ) are shown in Fig. 7. The dielectric relaxation characteristic of bismuth-

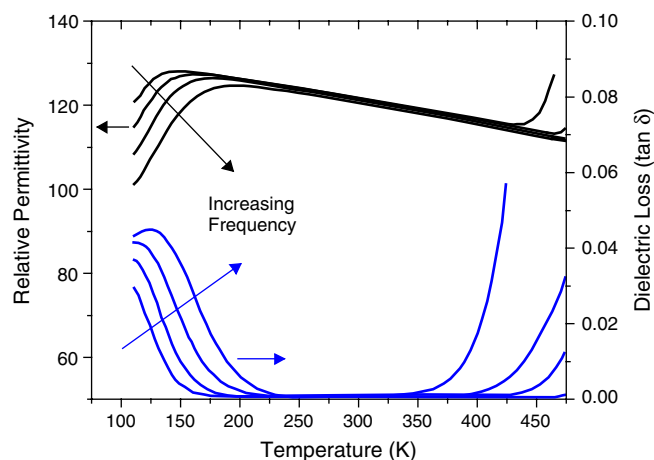


Fig. 7. Relative dielectric permittivity (corrected for porosity) and dielectric loss for the single-phase pyrochlore 0.4250:0.2800:0.2950  $\text{Bi}_2\text{O}_3\text{:Fe}_2\text{O}_3\text{:Nb}_2\text{O}_5$  ( $\text{Bi}_{1.657}\text{Fe}_{1.092}\text{Nb}_{1.150}\text{O}_7$ ) at frequencies (left to right) of 1, 10, 100 kHz and 1 MHz. Below 200 K the dielectric relaxation characteristic of bismuth-based pyrochlores is clearly observed; with increasing measuring frequency the peak in the dielectric loss shifts towards higher temperatures and the width of the dielectric loss peak increases. In the temperature region around 300 K the temperature coefficient of the relative permittivity is negative. The upturns at high temperatures indicate that the sample becomes conductive.

based pyrochlores is clearly observed [66–69]: with increasing measuring frequency, the peak of the dielectric loss shifts towards higher temperatures and the width of the dielectric loss peak increases. At 1 MHz, this pyrochlore exhibits a maximum relative dielectric permittivity of  $\sim 125$  at 200 K, and the peak of the dielectric loss occurs at  $T_m \sim 125$  K. When compared with the bismuth zinc niobate pyrochlore  $\text{Bi}_{1.5}\text{Zn}_{0.92}\text{Nb}_{1.5}\text{O}_{6.92}$  [68], the Fe analog exhibits a higher  $T_m$  but a lower dielectric constant. In addition, the upturns in the permittivity and loss above 350 K indicate that at higher temperatures the compound ceases to be insulating and becomes conductive. The nature of the conductivity is at present unclear; electrode-ceramic interface polarization processes may be involved, but different electrode materials and deposition methods were tested and identical results were obtained.

## 4. Conclusions

A study of subsolidus phase equilibria in the  $\text{Bi}_2\text{O}_3\text{--Fe}_2\text{O}_3\text{--Nb}_2\text{O}_5$  system ( $800\text{--}1075^\circ\text{C}$ , air) confirmed the formation of four ternary phases. Three of these phases have not been previously reported; i.e., Aurivillius-type  $\text{Bi}_3\text{Fe}_{0.5}\text{Nb}_{1.5}\text{O}_9$ , and  $\text{Bi}_8\text{Nb}_{18}\text{O}_{57}$ -related phases with compositions near  $\text{Bi}_{17}\text{Fe}_2\text{Nb}_{31}\text{O}_{106}$  and  $\text{Bi}_{17}\text{Fe}_3\text{Nb}_{30}\text{O}_{105}$ . The fourth phase is pyrochlore which forms an extensive solid solution region at stoichiometries that are ‘‘Bi-deficient’’ compared to conventional  $\text{A}_2\text{B}_2\text{O}_7$ -type formulations with Bi on the *A*-sites and Fe/Nb on the *B*-sites—the pyrochlore-type formulation  $\text{Bi}_2\text{FeNbO}_7$  is not included in this region. The location of the pyrochlore field suggests that  $\approx 4\text{--}15\%$  of the *A*-sites can be occupied by

$\text{Fe}^{3+}$ . Compared to analogous Bi–*M*–Nb–O pyrochlores with *M* = Zn, Mn, or Co, the Bi–Fe–Nb–O phase field is unique in shape and suggests that in this system the structure tolerates significantly lower concentrations of *B*-type ions on the *A*-sites and markedly higher *A*-site vacancy concentrations. These effects are attributed to the presence of trivalent Fe whereas in the other systems the *M* cations are present partially or fully in the divalent state. Observation of 442-type reflections in X-ray powder diffraction patterns indicated that all Bi–Fe–Nb–O pyrochlores form with site displacements, as found for the analogous systems with Zn, Fe, and Co instead of Fe. A structural refinement of the 0.4400:0.2700:0.2900 Bi<sub>2</sub>O<sub>3</sub>:Fe<sub>2</sub>O<sub>3</sub>:Nb<sub>2</sub>O<sub>5</sub> pyrochlore using neutron powder diffraction data is reported with the displacements modelled somewhat differently than those in Bi<sub>1.5</sub>Zn<sub>0.92</sub>Nb<sub>1.5</sub>O<sub>6.92</sub>. The results are consistent with a structural formula of Bi<sub>1.721</sub>Fe<sub>0.190</sub>(Fe<sub>0.866</sub>Nb<sub>1.134</sub>)O<sub>7</sub>. Apparently, from system to system and perhaps even within a given chemical system, variations in the chemistry of the *A*<sub>2</sub>O' network can drive differences in the details of the displacive behavior that often occurs in pyrochlores. Bi–Fe–Nb–O pyrochlores exhibited overall paramagnetic behavior with antiferromagnetic interactions at low temperature and the presence of some superparamagnetic effects; observed moments were depressed compared to the high-spin, spin-only value for Fe<sup>3+</sup>. Measurements of relative dielectric permittivity and dielectric loss of a Bi–Fe–Nb–O pyrochlore as a function of temperature and frequency revealed dielectric relaxation similar to that in the Bi–Zn–Nb–O system, and the onset of conductivity above 350 K. Bi–Fe–Nb–O pyrochlores were readily obtained as single crystals and also as textured thin films using pulsed laser deposition.

### Acknowledgments

We thank L.P. Cook for thermogravimetric analyses, N. Swanson for graphical representation of the phase diagram data, and R.D. Shull for helpful discussions. We thank I. Grey and N. Wilson for providing microprobe analytical data for single crystals of phases **A** and **B**. Pre-publication discussions and information exchange with R. Withers are duly noted and greatly appreciated. I.M. Pazos was supported in part by the National Science Foundation's Research Experience for Undergraduates (REU) program, Division of Materials Research.

### References

- [1] N.A. Spaldin, M. Fiebig, *Science* 309 (2005) 391.
- [2] V.E. Wood, A.E. Austin, *Magnetoelectric Interaction Phenomena in Crystals*, Gordon and Breach, London, 1975.
- [3] N.A. Hill, *J. Phys. Chem. B* 104 (2000) 6694 and references therein.
- [4] P. Baettig, N.A. Spaldin, *Appl. Phys. Lett.* 86 (2005) 012505 and references therein.
- [5] D.V. Efremov, J. Van den Brink, D.I. Khomskii, *Nat. Mater.* 3 (2004) 853.
- [6] C. Ederer, N.A. Spaldin, *Phys. Rev. B* 71 (2005) 060401(R) and references therein.
- [7] T. Kimura, S. Kawamoto, I. Yamada, M. Azuma, M. Takano, Y. Tokura, *Phys. Rev. B* 67 (2003) 180401(R) and references therein.
- [8] B.B. Van Aken, T.T.M. Palstra, A. Filippetti, N.A. Spaldin, *Nat. Mater.* 3 (2004) 164 and references therein.
- [9] M. Kenzelmann, A.B. Harris, S. Jonas, C. Broholm, J. Schefer, S.B. Kim, C.L. Zhang, S.W. Cheong, O.P. Vajk, J.W. Lynn, *Phys. Rev. Lett.* 95 (2005) 087206 and references therein.
- [10] O.P. Vajk, M. Kenzelmann, J.W. Lynn, S.B. Kim, S.W. Cheong, *Phys. Rev. Lett.* 94 (2005) 087601 and references therein.
- [11] M. Azuma, K. Takata, T. Saito, S. Ishiwata, Y. Shimakawa, M. Takano, *J. Am. Chem. Soc.* 127 (2005) 8889.
- [12] C.G. Bergeron, S.H. Risbud, *Introduction to Phase Equilibria in Ceramics*, American Ceramic Society, Westerville, 1984.
- [13] C.S. Barrett, *Structure of Metals*, first ed, McGraw-Hill, New York, 1943 (Chap. X).
- [14] C.R. Hubbard, Y. Zhang, R.L. McKenzie, *Certificate of Analysis, SRM 660*, National Institute of Standards and Technology, Gaithersburg, MD 20899, 1989.
- [15] R.F. Egerton, *Electron Energy Loss Spectroscopy in the Electron Microscope*, Plenum Press, New York, 1996.
- [16] A. Auhtor, *Phase Equilibria Diagrams (formerly Phase Diagrams for Ceramists)*, The American Ceramic Society, Westerville, OH, 2006 (Figs. 324, 327e, EC-156).
- [17] V.K. Trunov, L.M. Kovba, Z.Y. Pol'shchikova, *Russ. J. Inorg. Chem.* 13 (1968) 786.
- [18] N. Niizeki, M. Wachi, *Z. Kristallogr. Kristallgeom. Kristallphys. Kristalchem.* 127 (1968) 173.
- [19] S.V. Kiselev, R.P. Ozerov, G.S. Zhdanov, *Sov. Phys. Dokl.* 7 (1963) 742.
- [20] C. Michel, J.-M. Moreau, G.D. Achenbach, R. Gerson, W.J. James, *Solid State Commun.* 7 (1969) 701.
- [21] J.R. Teague, R. Gerson, W.J. James, *Solid State Commun.* 8 (1970) 1073.
- [22] D.C. Craig, N.C. Stephenson, *J. Solid State Chem.* 15 (1975) 1.
- [23] G.D. Achenbach, W.J. James, R. Gerson, *J. Am. Ceram. Soc.* 50 (1967) 437.
- [24] R.S. Roth, J.L. Waring, *J. Res. NBS* 66A (6) (1962) 451.
- [25] R.L. Withers, C.D. Ling, S. Schmid, *Z. Kristallogr.* 214 (1999) 296.
- [26] C.D. Ling, R.L. Withers, S. Schmid, J.G. Thompson, *J. Solid State Chem.* 137 (1998) 42.
- [27] M. Valant, B. Jancar, U. Pirnat, D. Suvorov, *J. Eur. Ceram. Soc.* 25 (2005) 2829.
- [28] U. Pirnat, M. Valant, B. Jancar, D. Suvorov, *Chem. Mater.* 17 (2005) 5155.
- [29] C.D. Ling, M. Johnson, *J. Solid State Chem.* 177 (2004) 1838.
- [30] M. Valant, D. Suvorov, *J. Am. Ceram. Soc.* 86 (2003) 939.
- [31] M. Valant, D. Suvorov, *J. Am. Ceram. Soc.* 87 (2004) 1056.
- [32] E.M. Levin, R.S. Roth, *J. Res. NBS* 68A (1964) 189.
- [33] J.G. Thompson, A.D. Rae, R.L. Withers, D.C. Craig, *Acta Cryst. B* 47 (1991) 174.
- [34] M.A. Subramanian, G. Aravamudan, G.V.S. Rao, *Prog. Solid State Chem.* 15 (1983) 55.
- [35] T.A. Vanderah, I. Levin, M.W. Lufaso, *Eur. J. Inorg. Chem.* 14 (2005) 2895.
- [36] W. Somophon, V. Ting, Y. Liu, R.L. Withers, Q. Zhou, B.J. Kennedy, *J. Solid State Chem.* 179 (2006) 2462.
- [37] Ismunandar, B.J. Kennedy, B.A. Hunter, *Mater. Res. Bull.* 34 (1999) 1263.
- [38] B.J. Kennedy, *Physica B* 241 (1997) 303.
- [39] M. Bruhwiler, S.M. Kazakov, N.D. Zhigadlo, J. Karpinski, B. Batlogg, *Phys. Rev. B* 70 (2004) 020503.
- [40] Y. Torii, K. Hasegawa, *Bull. Chem. Soc. Japan* 50 (1977) 2638.
- [41] A. Ramanan, J. Gopalakrishnan, C.N.R. Rao, *J. Solid State Chem.* 60 (1985) 376.
- [42] G. Filoti, M. Rosenberg, V. Kuncser, B. Seling, T. Fries, A. Spies, S. Kemmler-Sack, *J. Alloys Compd.* 268 (1998) 16.

- [43] Z.G. Zou, J.H. Ye, H. Arakawa, *J. Mol. Catal. A—Chem.* 168 (2001) 289.
- [44] Z.G. Zou, J.H. Ye, H. Arakawa, *J. Mater. Res.* 16 (2001) 35.
- [45] I.V. Piiir, D.A. Prikhodko, S.V. Ignatchenko, A.V. Schukariov, *Solid State Ionics* 101–103 (1997) 1141.
- [46] I. Levin, T.G. Amos, J.C. Nino, T.A. Vanderah, C.A. Randall, M.T. Lanagan, *J. Solid State Chem.* 168 (2002) 69.
- [47] T.A. Vanderah, M.W. Lufaso, A.U. Adler, I. Levin, J.C. Nino, V. Provenzano, P.K. Schenck, *J. Solid State Chem.*, in press.
- [48] T.A. Vanderah, T. Siegrist, M.W. Lufaso, M.C. Yeager, J.C. Nino, S. Yates, *Eur. J. Inorg. Chem.*, in press.
- [49] D.M. Pease, S.D. Bader, M.B. Brodsky, J.I. Budnick, T.I. Morrison, J. Zaluzec, *Phys. Lett. A* 114 (1986) 491.
- [50] D.H. Pearson, C.C. Ahn, B. Fultz, *Phys. Rev. B* 47 (1993) 8471.
- [51] C.C. Calvert, A. Brown, R. Brydson, *J. Electron Spectrosc. Relat. Phenom.* 143 (2005) 173.
- [52] L.A.J. Garvie, P.R. Buseck, *Nature* 396 (1998) 667.
- [53] M. Ganne, K. Toyama, *Mat. Res. Bull.* 10 (1975) 1313.
- [54] S. Uma, S. Kodialam, A. Yokochi, N. Khosrovani, M.A. Subramanian, A.W. Sleight, *J. Solid State Chem.* 155 (2000) 225.
- [55] M. Avdeev, M.K. Haas, J.D. Jorgensen, R.J. Cava, *J. Solid State Chem.* 169 (2002) 24.
- [56] L.Q. Li, B.J. Kennedy, *Chem. Mater.* 15 (2003) 4060.
- [57] Ismunandar, T. Kamiyama, K. Oikawa, A. Hoshikawa, B.J. Kennedy, Y. Kubota, K. Kato, *Mater. Res. Bull.* 39 (2004) 553.
- [58] R.L. Withers, T.R. Welberry, A.K. Larsson, Y. Liu, L. Noren, H. Rundlof, F.J. Brink, *J. Solid State Chem.* 177 (2004) 231.
- [59] I.E. Grey, W.G. Mumme, A structural model refined using single-crystal XRD data was found to be consistent with that reported here using neutron powder diffraction data, private communication.
- [60] N.E. Brese, M. O’Keeffe, *Acta Crystallogr. B* 47 (1991) 192–197. with updated Ro parameters <[http://www.ccp14.ac.uk/ccp/web-mirrors/i\\_d\\_brown/](http://www.ccp14.ac.uk/ccp/web-mirrors/i_d_brown/)>
- [61] A.L. Hector, S.B. Wiggin, *J. Solid State Chem.* 177 (2004) 139.
- [62] R.B. Goldfarb, *Concise Encyclopedia of Superconducting and Magnetic Materials*, Pergamon Press, Oxford, 1992.
- [63] J.E. Greedan, *J. Mater. Chem.* 11 (2001) 37.
- [64] A.P. Ramirez, A. Hayashi, R.J. Cava, R. Siddharthan, B.S. Shastry, *Nature* 399 (1999) 333.
- [65] R. Siddharthan, B.S. Shastry, A.P. Ramirez, A. Hayashi, R.J. Cava, S. Rosenkranz, *Phys. Rev. Lett.* 83 (1999) 1854.
- [66] J.C. Nino, M.T. Lanagan, C.A. Randall, *J. Appl. Phys.* 89 (2001) 4512.
- [67] D.P. Cann, C.A. Randall, T.R. Shroud, *Solid State Commun.* 100 (1996) 529.
- [68] S. Kamba, V. Porokhonsky, A. Pashkin, V. Bovtun, J. Petzelt, J.C. Nino, S. Troler-McKinstry, M.T. Lanagan, C.A. Randall, *Phys. Rev. B* 66 (2002) 54106.
- [69] J.C. Nino, H.J. Youn, M.T. Lanagan, C.A. Randall, *J. Mater. Res.* 17 (2002) 1178.